Research Article

Numerical Simulation of Landslide-Tsunami Involving Different Impact Angles

Jizhixian Liu[1, *], Yujie Zhang[2] and Chaoyue Yang[3]

[1]Hubei Engineering University, Xiaogan, 432000, China
[2]Central-South Architectural Design Institute Co.,Ltd, Wuhan, 430000, China
[3]China Three Gorges Construction Engineering Corporation, Beijing,100000, China

___

Abstract

Landslide-tsunami formed by landslide impacting into water severely threatens the life and property safety of residents along coastal areas. The slide impact angle of landslide (α) is an essential parameter in landslide-tsunami prediction. Many studies have discussed the response laws of formation features of landslide-tsunami to the comprehensive effect of α and several other factors. However, the influencing laws of α on landslide-tsunami features vary and are even contradictory among different studies. To determine the independent effects of α on wave generation, this study used a numerical simulation correction on the correction utilized smoothed particle hydrodynamics (SPH) method, which verified the efficacy of SPH method in simulating landslide-tsunamis. Next, three groups of landslide-tsunami numerical simulation tests under different α (10°, 20°, and 30°) were implemented to analyze the influencing laws of α on water motion features, water occupation by the landslide, and energy conversion law thoroughly. Results demonstrate that the SPH method could simulate the generation and propagation of landslide-tsunami well, achieving a relatively high simulation accuracy. The landslide and water movements in the three groups of numerical simulations are similar. As α increases from 10° to 30° successively, the rate of water occupation by the landslide decreases gradually, but the volume of water occupied by the landslide increases. The maximum occupational volume reaches 7.91 times as that of landslide. After the landslide enters the water, the energy attenuation rate increases with the increment of α, and it reaches the lowest at α = 10°. Generally, with α increasing, the amplitude of the first wave decreases, while the amplitude of the second wave increases. The proposed conclusions provide some references to constructing the landslide-tsunami prediction model.

Keywords: Landslide-tsunami, SPH method, Slide impact angle, Energy conversion law, Water occupation by the landslide

___

1. Introduction

Landslide-tsunami is a vital hazard in lakes, reservoirs, fjords, and sea. Losses caused by landslide-tsunami have become essential to landslide-induced losses [1]. For example, more than 2.7 million m³ of sliding mass impacted a reservoir in Italy in 1963, and the tsunami caused more than 2,000 deaths upstream and downstream [2]. In 2014, a landslide occurred in Lake Asja, Ice Island, and a vast landslide-tsunami was generated. The landslide-tsunami wave propagated on the lake for nearly 3 km, and the vertical height of the wave on banks reached 60-80 m [3]. In 2014, a glacier collapse occurred in Eqip Sermia Glacier in the west of Greenland, and it generated a 50 m high landslide-tsunami wave after the collapsed glacier entered the water [4]. According to statistics, the cumulative deaths in landslide-tsunami events exceed 58,000, accompanied by considerable economic losses [1]. Presently, the prediction and emergency treatment of landslide-tsunamis are among the most concerning problems for researchers and disaster management departments.

The generation mechanism of landslide-tsunamis is a crucial research focus because it determines the level of disaster intensity associated with these events. In previous studies, landslide-tsunami is generated upon the impact of a landslide with some volume into water bodies, giving rise to a multiphase transient flow process that involves solid, liquid, and gas phases [5]. The generation of landslide-

tsunami is influenced by many parameters, mainly including thickness, width, length, volume, mass of landslide, water depth, impact velocity, and slide impact angle [1,6-8]. In relevant studies, the thickness, width, length, volume, mass, and the impact velocity, correlate positively with the features of landslide-tsunami waves. In contrast, water depth negatively correlates with landslide-tsunami wave features [8-11]. Nevertheless, dispute over the influencing laws of slide impact angle on landslide-tsunami features still exists. Most relevant studies focus on the response laws of landslide-tsunami generation features to the collaborative effect of slide impact angle and other influencing factors. Some studies reported that landslide-tsunami features intensified with the increase in slide impact angle, but some studies reached the opposite conclusions. How the slide impact angle influences the generation of landslide-tsunami independently has to be studied further. Thus, landslide-tsunami numerical simulation tests were set-up by changing the slide impact angle of the landslide alone and carried out by the control variable using a numerical simulation method based on smoothed particle hydrodynamics (SPH) method. The influencing laws of slide impact angle on landslide-tsunami features were analyzed from the wave motion features, the volume of water occupied by the landslide, and energy transmission. The conclusions of this study are expected to provide references for parameter selection to study the feature prediction model of landslide-tsunami.

___

2. State of the art

The slide impact angle of landslide (α) is an important influencing factor of landslide-tsunami features, and it determines the impact mode between the landslide and the water body. It affects wave features generated by the interaction between landslides and water bodies. In the past decades, many studies on the influences of α have been published, and some research conclusions have been drawn. Kamphuis and Bowering [12] performed a two-dimensional laboratory experimental study of landslide-tsunami in a 45 m (length) × 1 m (width) wave channel. For the first time, findings show that the conversion rate from landslide energy to wave energy was 10%–50%. Moreover, the energy conversion rate declined gradually with the increase in α. Ataie-Ashtiani and Nik-Khah [13] reached the same conclusion on the relationship between α and energy conversion through a two-dimensional laboratory test. By analyzing the results of 211 landslide-tsunami laboratory tests, Heller and Hager [7] concluded that landslide-tsunami features declined with the increase in α. Mulligan and Take [14] deduced a negative correlation between α and landslide-tsunami features after analyzing the momentum transfer of waves based on laboratory tests. Through a two-dimensional experimental study, Bullard et al. [15] studied the relationship between wave features generated by high-liquidity landslide and α. They verified the research conclusions of Mulligan and Take [14]. In the five studies mentioned above, the landslide-tsunami laboratory tests are completed in a two-dimensional wave channel, thereby simplifying many test parameters. As a result, the test results exhibited great differences from a real landslide-tsunami. For three-dimensional laboratory tests of landslide-tsunami, Evers et al. [8] carried out 74 three-dimensional laboratory tests of landslide-tsunami in a 4.5 m × 8.0 m pool. They observed that the slide impact zone was positively correlated with α, but wave features were negatively correlated with α. On the contrary, Huang et al. [16] proposed a prediction model of landslide-tsunami features from a three-dimensional physical similarity test of rock mass in water and believed that α was proportional to the first wave amplitude. Bougouin et al. [17] conducted laboratory tests of landslide-tsunami in grain flows and concluded that the primary wave features in the near-field region were positively related to α. Besides, Bregoli et al. [10] carried out three-dimensional landslide-tsunami tests within the α range of 0°-27.8° and believed that the wave prediction model could ignore the influences of α. Similarly, Yavari-Ramshe and Ataie-Ashtiani [18] proposed a landslide-tsunamis wave height prediction model through a numerical simulation study, which excluded α. Through a statistical summary of empirical formulas of wave features and a sensitive analysis of influencing factors, Sabeti and Heidarzadeh [6] found that landslide-tsunami features presented complicated features with the increase in α rather than a monotonous increase or decrease.

Based on the above studies, landslide-tsunami features are mainly influenced by multiple factors. Existing studies mainly focus on the collaborative influences of various factors on landslide-tsunami, but few emphasize the independent effects of α on landslide-tsunami features. Different comprehensive studies conclude that the influencing laws of α vary. Contradictions have been raised among many research conclusions. Some conclusions show a negative correlation between landslide-tsunami features and α, while some report a positive correlation, and some

even believe that the influences of α on wave features could be ignored or are complicated. For this reason, numerical simulation tests of landslide-tsunami were carried out in this study by using the SPH and control variable methods. It focuses on studying the influences of α on wave features. The influencing laws of α on landslide-tsunami features were summarized deeply by observing the generation of landslide-tsunamis and analyzing the water occupied by the landslide and the energy conversion of the landslide. This study offers reference points for parameter selection in the landslide-tsunami prediction model.

The remainder of this study is organized as follows. Section 2 introduces the principle of the SPH numerical simulation method, the construction of the numerical simulation for the calibration test, and the set-up of the numerical simulation test. Section 3 compares the numerical simulation results and the existing laboratory test results and analyzes the calculation accuracy of numerical simulation in this study. Section 4 analyzes landslide movement and water motion process under three slide impact angles, water occupation by landslide, as well as influencing laws of α on energy conversion of landslide. Section 5 summarizes the major conclusions.

3. Methodology

3.1 Basic theory of SPH

This study mainly employed the SPH method for numerical simulation calculation. The numerical simulation solver of landslide-tsunami used the open-source code DualSPHysics v5.0.4 of the SPH algorithm [19]. SPH is a Lagrange meshless method applicable to simulating intensive free surface flow [20,21]. SPH algorithm discretizes continuum by using a group of material points (particles) with physical properties (e.g., mass, density, and pressure). Due to interaction with adjacent particles, these properties may change with time. Any physical variable (f) of fluid particle a (subscript a) at the position $\mathbf{x}_a$ can be approximated by the integral expression method of the smooth kernel (or weighted) function $W\left(\mathbf{x}_a - \mathbf{x}, h_{\mathrm{p}}\right)$ [22].

$$f\left(\mathbf{x}_a\right) = \int_{\Omega} f(\mathbf{x}) W\left(\mathbf{x}_a - \mathbf{x}, h_{\mathrm{p}}\right) d\mathbf{x} \tag{1}$$

where h_{p} is the smooth length of the influence domain of the defined internal kernel. Ω is the computational domain, and $\mathbf{x}$ is the integral position vector. The integral approximate value in Eq. (1) is based on discontinuous and discrete forms of adjacent particles:

$$f\left(\mathbf{x}_a\right) \approx \sum_b f\left(\mathbf{x}_b\right) \frac{m_b}{\rho_b} W\left(\mathbf{x}_{ab}, h_{\mathrm{p}}\right) \tag{2}$$

where the sum was expanded to all particles in the domain. In $\mathbf{x}_a - \mathbf{x}_b$, $\mathbf{x}_a$ and $\mathbf{x}_b$ are the position vectors of fluid particles a and b (subscript b). m_a and ρ_a are the mass and density, respectively. The kernel functional values between particles a and b are abbreviated as W_{ab}, which can use a series of kernel functions, including the cubic spline function [23] and Wendland kernel function [24]. In this study, the Wendland kernel function was applied.

$$W\left(\mathbf{x}_{ab}, h_p\right) \approx \alpha_D (1 - \frac{q}{2})^4 (2q+1) \qquad 0 \leq q \leq 2 \qquad (3)$$

where α_D is equal to $7/(4\pi h^2)$ in 2D simulation, and it is equal to $21/(16\pi h^3)$ [20,21] in 3D simulation. The SPH solver in current study is mainly based on discretized Navier–Stokes and continuity equation [25].

$$\frac{d\mathbf{u}}{dt} = -\frac{\nabla p}{\rho} + \mathbf{g} + \boldsymbol{\Gamma} \qquad (4)$$

$$\frac{d\rho}{dt} = -\rho \nabla \mathbf{u} \qquad (5)$$

where $\mathbf{u}$ is the speed field vector, p is pressure, ρ is density, g is the gravitational acceleration vector, and $\boldsymbol{\Gamma}$ considers the dissipation term.

In the SPH method, the dissipation term includes artificial viscosity, laminar viscosity, and laminar + subparticle scale (SPS) turbulence [26]. In this study, particle motion a was described by using the discrete equation (5) of artificial viscosity [22] as follows:

$$\frac{d\mathbf{u}_a}{dt} = -\sum_b m_b \left(\frac{p_a + p_b}{p_b \cdot p_a} + \Pi_{ab}\right) \nabla_a W_{ab} + \mathbf{g} \qquad (6)$$

where ∇_a is the kernel gradient related with the coordinates of particle a. ρ_a and ρ_b are density. p_a and p_b are the corresponding pressure. Π_{ab} is the artificial viscosity term, as shown in Eq. (7)

$$\Pi_{ab} = \begin{cases} \dfrac{-\alpha \overline{c_{ab}} \mu_{ab}}{\overline{\rho_{ab}}} & \mathbf{u}_{ab} \cdot \mathbf{x}_{ab} < 0 \\ 0 & \mathbf{u}_{ab} \cdot \mathbf{x}_{ab} > 0 \end{cases} \qquad (7)$$

where $\overline{c_{ab}} = 0.5(c_a + c_b)$ is the average sound velocity. c_a and c_b are the sound velocity. $\overline{\rho_{ab}} = 0.5(c_a + c_b)$ is the average density. $\mu_{ab} = h_p \mathbf{u}_{ab} \cdot \mathbf{x}_{ab} / (\mathbf{x}_{ab}^2 + \eta^2)$ is the parameter added to prevent outliers, where $\eta^2 = 0.01 h_p^2$ [22]. α is an artificial coefficient, and its values in this numerical simulation is 0.01. In $\mathbf{u}_{ab} = \mathbf{u}_a - \mathbf{u}_b$, $\mathbf{u}_a$ and $\mathbf{u}_b$ are velocity vectors.

In this study, the traditional weak compressible SPH method was applied to avoid the necessity of solving Poisson's equation [22]. The following equation estimates the relationship between pressure and density of fluid.

$$p_a = \frac{c_0^2 \rho_0}{\gamma} \left[\left(\frac{\rho_a}{\rho_0}\right)^\gamma - 1\right] \qquad (8)$$

where $\rho_0 = 1000$ kg/m^3 is a reference density, and $\gamma = 7$ [22] for fluid. c_0 is the numerical sound velocity. Given that the compressibility of fluid is determined by c_0, it shall be set at least 10 times the maximum flow velocity (here, $c_0 = 71.2$m/s). This approach restricts the relative density to

be lower than 1%, thus meeting the uncompressible requirement of water [26].

In Eq. (8), the dissipation term of velocity is discretized in SPH, and it is written as:

$$\frac{d\rho_a}{dt} = \sum_b m_b \mathbf{u}_{ab} \cdot \nabla_a W_{ab} + \delta h_p c_0 \sum_b \boldsymbol{\Psi}_{ab} \cdot \nabla_a W_{ab} \frac{m_b}{\rho_b} \qquad (9)$$

where

$$\boldsymbol{\Psi}_{ab} = 2\left(\rho_b - \rho_a\right) \frac{\mathbf{x}_{ab}}{\left\| \mathbf{x}_{ab} \right\|^2} \qquad (10)$$

According to the suggestions of DualSPhysics parameter selection, δ is a free parameter.

3.2 Numerical model verification of landslide-tsunami

In this study, the laboratory test of landslide-tsunami (Liu et al. [27]) was applied for numerical simulation verification to interpret the reasonability of numerical simulation parameter selection in the SPH method, and to verify the effectiveness of the SPH method in simulating the generation and propagation of landslide-tsunami. In this laboratory test, the length, width, thickness, and impact velocity were $l = 0.2$ m, $b = 0.4$ m, $s = 0.1$ m, and $v = 2.0$ m/s. The water depth was $h = 0.29$ m, and $\alpha = 30°$.
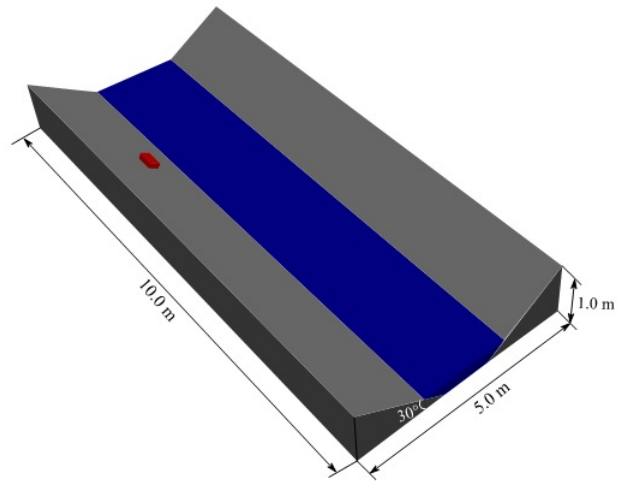
Fig. 1. Schematic diagram of three-dimensional landslide-tsunami numerical model

For the geometric model of landslide in the numerical model, α, h, and water width all applied the sizes consistent with laboratory tests. Considering that the SPH method consumes considerably high computing resources, the length of the water pool decreased from 22 m to 10 m (Fig. 1). Based on gravitational acceleration, the impact speed (v) of the numerical simulation specimen reached 2.0 m/s, and the rigid block was placed on the sliding surface, which was 0.22 m higher than the water surface. The whole numerical model was composed of particles. When the maximum wave height (H_M) is 10 times the particle spacing, that is $d_p = H_M/10$, the generation and propagation of landslide-tsunami, which are simulated and calculated by this solver, are optimal. In the selected laboratory test, H_M was 0.09 m. After comprehensive consideration, the particle spacing of the numerical model was $d_p = 10$ mm. After modeling, the model involved 13,228,982 particles. Specifically, the water

boundaries, fluid, and landslide block were composed of 9,784,580, 3,434,562, and 9,840 particles, respectively. The numerical model is shown in Fig. 1. Numerical parameters and constants were set similarly to those of Heller et al. [25]. The time-stepping algorithm used symplectic and boundary conditions and opted for dynamic boundaries. Courant–Friedrichs–Lewy number was 0.2, and the sound velocity coefficient was 17. DualSPHysics v5.0.4 numerical parameters set by other parameters are introduced in Section 3.1. In this study, the GPU of DualSPHysics v5.0.4 open-

source code was operated on a PC equipped with 12 GB memory and a GeForce Titan Xp GPU. The stepping time was 0.01 s, and results were outputted every 0.05 s. The total calculation time was 10 s. The landslide-tsunami features calculated in the numerical simulation were mainly measured by the post-processing tool of DualSPHysics, and nine monitoring points were set. The locations of these monitoring points are shown in Fig. 2.
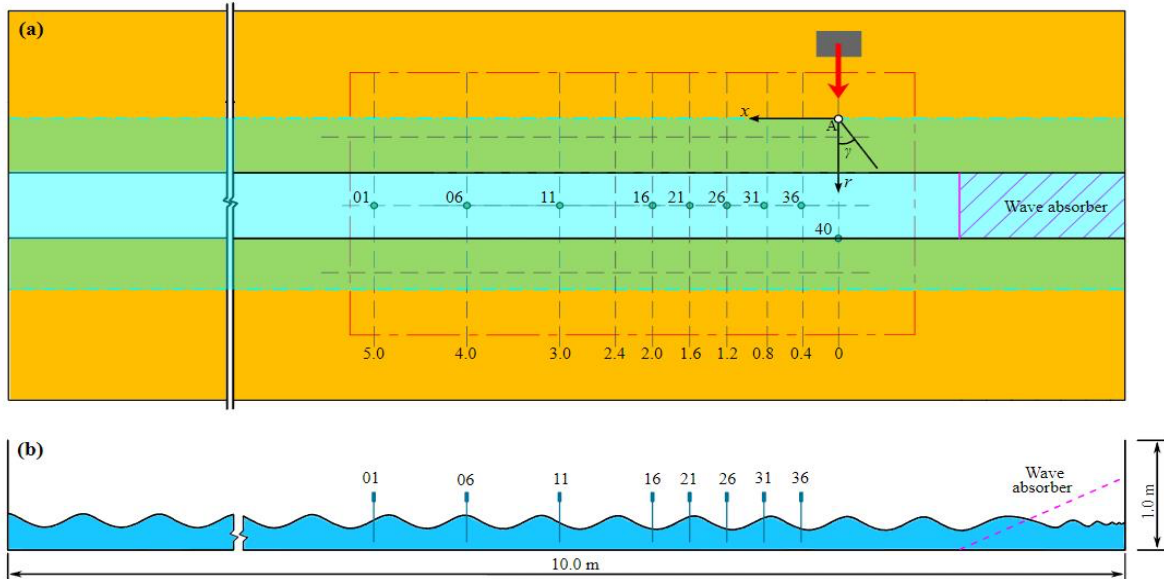
Fig. 2. Numerical simulation model of landslide-tsunami and layout of wave monitoring points
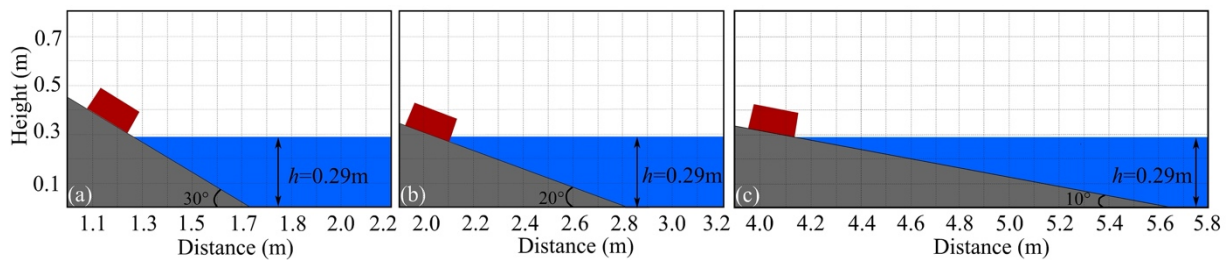
Fig. 3. Entry sections of landslide-tsunami in numerical simulation under different slide impact angles

3.3 Numerical test schemes of landslide-tsunami

α has remarkable influences on affecting the process of landslide and solid-liquid energy conversion. To disclose the response laws of landslide-tsunami features to α thoroughly, three groups of numerical simulation tests (e.g., G1, G2, and G3) were designed and carried out using a single control variable method based on the SPH method. Among these three test conditions, landslide volume was set at 0.4 m × 0.2 m × 0.1 m. Moreover, the impact velocity of landslide was 2.0 m/s. h = 0.29 m, and α = 10°, 20°, and 30°. The specific numerical simulation test schemes are listed in Table 1. The entry sections of landslide-tsunami numerical models under three slide impact angles are shown in Fig. 3.

Table 1. Numerical simulation test parameters

No.	Landslide size (b × l × s)	Impact angle α	Water depth h	Designed velocity v	Numerical velocity
G1	0.4 m × 0.2 m × 0.1 m	30°	0.29 m	2.0 m/s	1.977 m/s
G2	0.4 m × 0.2 m × 0.1 m	20°	0.29 m	2.0 m/s	2.045 m/s
G3	0.4 m × 0.2 m × 0.1 m	10°	0.29 m	2.0 m/s	2.050 m/s

4. Result analysis and discussion

4.1 Analysis of numerical simulation verification results

4.1.1 Landslide velocity reproduction in tests

According to the numerical simulation model in Section 3.2, the variation laws of v with time throughout the impact of landslide into water were analyzed. Fig. 4 shows that when t = 0 s, the landslide in the numerical simulation begins to slide down under the action of gravity. v = 0.85 m/s at t = 0.3 s, v = 1.06 m/s at t = 0.35 s, and v = 1.58 m/s at t = 0.45 s. v presents a linear growth with increased movement distance and an average acceleration of 4.25 m/s². The landslide begins to collide with water after acceleration sliding for 0.55 s (Fig. 4e). At this moment, the landslide reaches the maximum velocity v = 1.98 m/s, which has an error of −1.0% with the design value (2.0 m/s) and an error of −3.4% with the practical velocity (2.05 m/s) of the laboratory test. After touching the water surface, the landslide begins to decelerate due to water resistance and floating forces, continuously sliding downward along the slope. It arrives at the pool bottom at t = 0.9 s (Fig. 4.) with v = 1.22 m/s. Subsequently, it continues moving forward and is

completely static in water until $t = 1.9$ s. Based on the above analysis, the SPH method has good adaptability in selecting numerical parameters in DualSPHysics v5.0.4 solver. It reproduces the impacting process of landslide into water in the laboratory test.
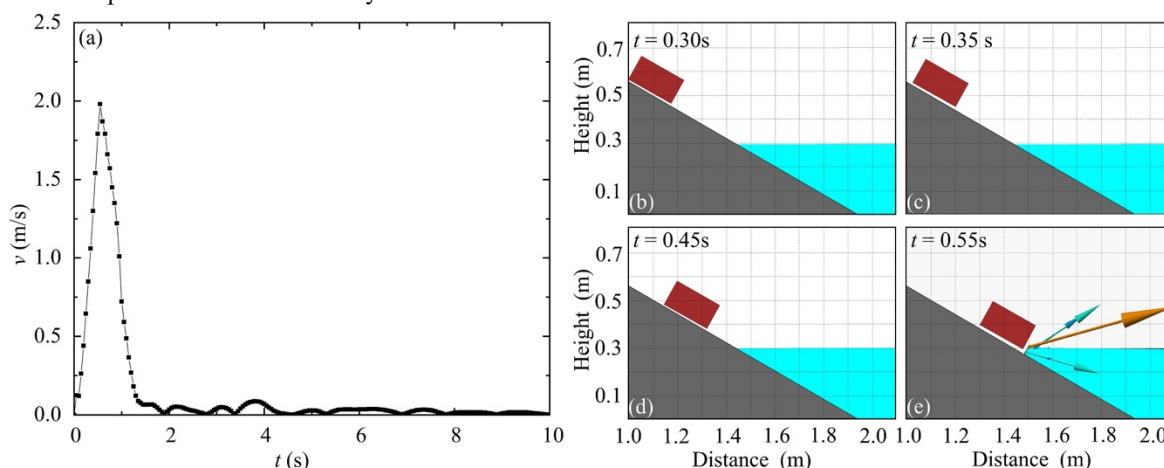
Fig. 4. (a) Variation in leading edge velocity of landslide with time; (b-e) Sliding process of landslide in numerical simulation

4.1.2 Landslide-tsunami feature simulation

According to the numerical simulation calculation results of landslide-tsunami in Section 3.2, the numerical simulation and laboratory test results of landslide-tsunami features at different monitoring points are compared carefully. The comparison of landslide-tsunamis wave profiles recorded by CWG40 at the entry section of landslide in numerical simulation and laboratory test are shown in Fig. 5(a). The wave amplitude time sequence chart in numerical simulation fits well with the laboratory test results. In particular, the numerical simulation and laboratory test results of the maximum wave amplitude a_{cM} are 0.0465 m and 0.0448 m, respectively, showing a deviation of 3.79%. The numerical simulation and laboratory test results of the maximum wave trough a_{tM} are −0.0319 m and −0.0336 m, respectively, with an error of −5%. The numerical simulation and laboratory test results are 0.0784 m, without deviation. The comparison of propagation attenuation of landslide-tsunami wave in river center in numerical simulation and laboratory test is shown in Figs. 5(b–i). Generally, the numerical model simulates the propagation attenuation process of landslide-tsunami waves. The numerical results of propagation attenuation of the first waves at all monitoring points agree well with the laboratory test results. Moreover, Fig. 5 shows that the third and fourth waves at most monitoring points in numerical simulation are highly similar to the variation trend of laboratory tests, but great differences in waveforms of follow-up wave trains were observed. The laboratory test result of wave crest is usually higher than the numerical simulation result and the maximum difference reaches 67% (Fig. 5e). This result is mainly because the water boundary in the laboratory test is longer than that in numerical model, resulting in different influences of the reflected wave of follow-up wave field on landslide-tsunami waves.

The statistical analysis of numerical calculation and laboratory test results of maximum wave amplitude a_{cM} and wave height H_M in the center of the water pool are shown in Fig. 6. According to previous theoretical studies and

laboratory experimental studies, a_{cM} attenuates with the increase in propagation distance x. In other words, $a_{cM}(x) \mu (x)^i$, where i is the attenuation index of propagation waves. According to the relations between a_{cM} and x in numerical simulation and laboratory test, it is estimated that i is −0.53 in numerical simulation and −0.47 in laboratory test, showing a deviation of −12.8%. The attenuation coefficients (i) of H_M in numerical simulation and laboratory test are −0.66 and −0.55, respectively, showing an error of −20%. This finding reflects that the SPH method and numerical simulation parameters could simulate the propagation attenuation of landslide-tsunami well.

4.2 Generation and energy conversion law of landslide-tsunami analysis

4.2.1 Analysis of landslide and water movement features

Monitoring the whole process of the rigid block from a static state to water entry under three test conditions in Section 3.3 can provide essential data to analyze the movement features of landslides. Given that the initial positions of landslides vary under the three conditions, the variations in the actual impact velocity of the landslide with time in numerical simulation are shown in Fig. 7. The designed impact velocity of landslide is 2.0 m/s, and the calculated values in numerical simulation under three conditions are listed in Table 1. The maximum error between the calculated result and the designed value is 2.5%. The movements of the landslide from a static position to acceleration and then to the designed velocity under G1 and G2 are similar. In contrast, the acceleration of landslide under G3 is far lower. After impacting into the water, the landslide velocity begins to decelerate. Moreover, the deceleration process of the landslide varies under three conditions. The deceleration rate of the landslide is positively related to α.
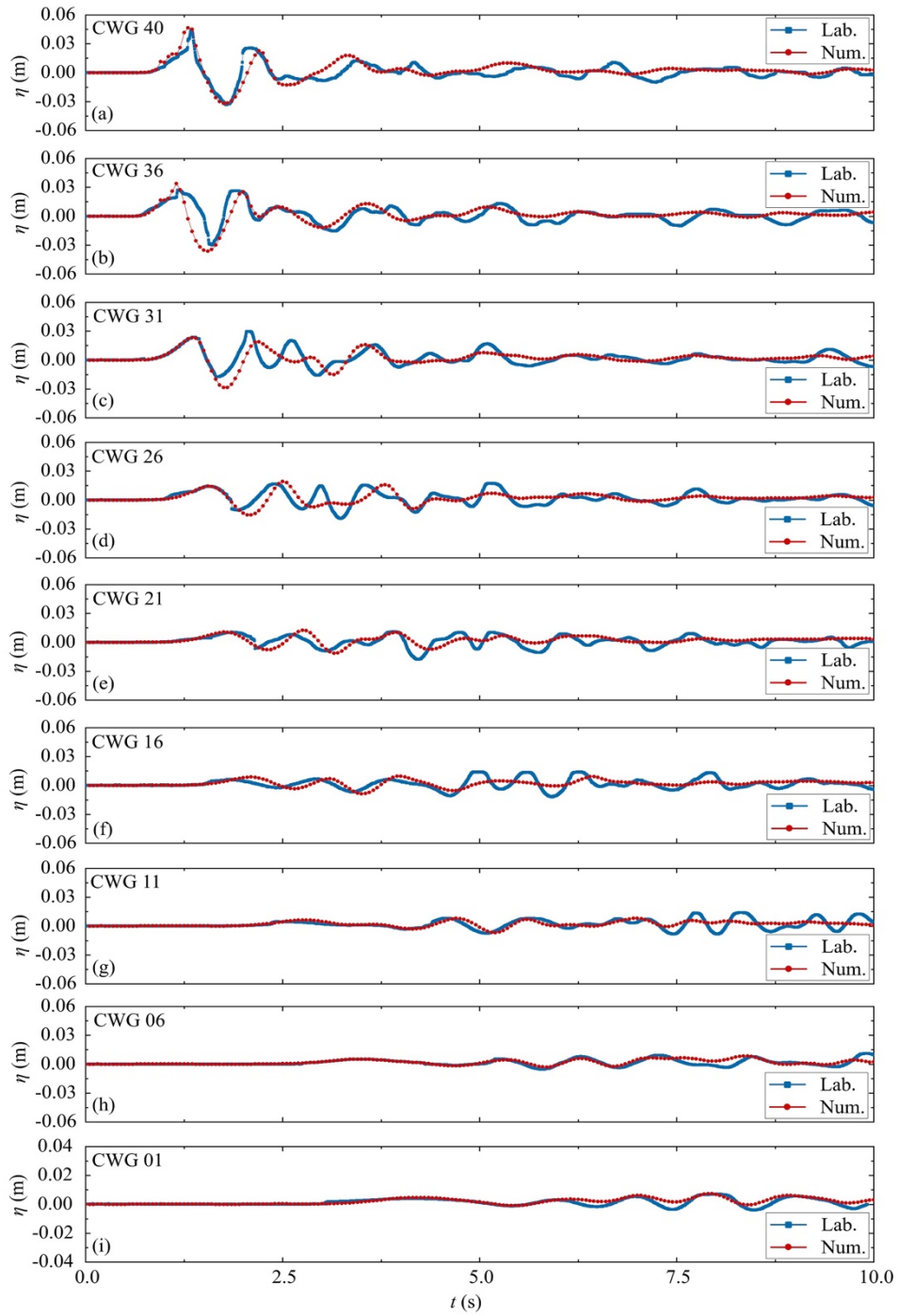
Fig. 5. Comparison of wave profiles at monitoring points in river center between laboratory test and numerical simulation
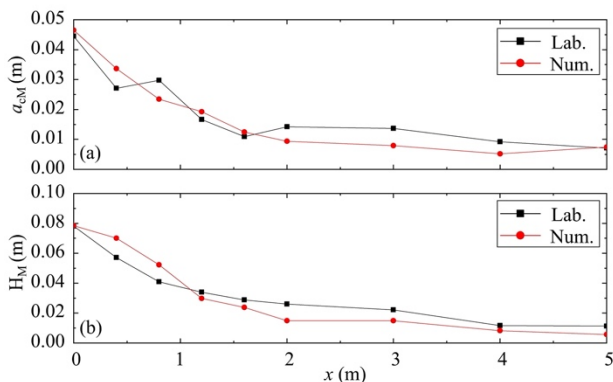
Fig. 6. Comparison of variations in (a) maximum wave peak a_{cM} and (b) maximum wave height H_M
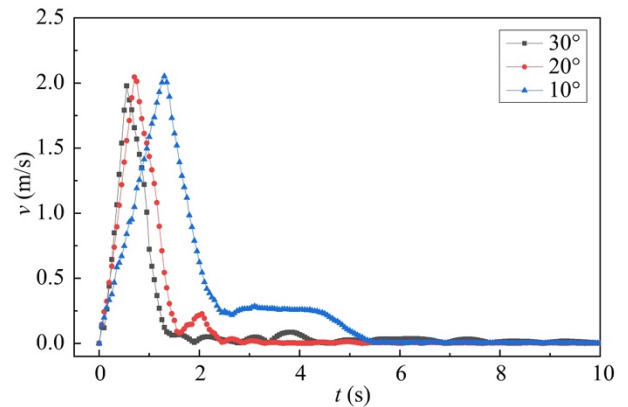
Fig. 7. Variations in landslide velocity with time in numerical simulation under three conditions

According to the observation of numerical simulation results, the movements of landslide and water under three slide impact angles are similar. Fig. 8 depicts that when the landslide begins to impact the water, it occupies some volume of water. Considering that water is a kind of uncompressible fluid, the water body may deform significantly, jumps out of the water surface, and form a water tongue upon the thrust of the landslide. When the water tongue collapses, the water body rises forward and toward the surrounding directions, thereby forming the first wave crest gradually. Air enters into the water body in the impacting process, and the generation zone of landslide-tsunami is a three-phase field of solid–liquid–gas mixing. A large cavity forms on the back of the water body to separate the landslide and fluid. Some water bodies are dragged or occupied by the landslide and continue to move along the main sliding direction, thereby generating the first wave trough gradually. Due to the air involvement, the second wave generation becomes complicated. The water occupied by the landslide reflows and converges at the posterior central line of the landslide gradually in the manner of impacting. As the landslide moves forward continuously, the water bodies that surround it collapse, thus compressing the air cavity constantly until being broken. After breaking the air cavity, air in water forms abundant bubbles that spill over the water surface. Turbulence is formed behind the landslide, which rises gradually and moves toward surrounding areas. Some begin to make annular propagation toward the opposite bank, starting the second wave crest gradually. As water movement continues, water bodies form the second wave trough under gravity. After the first and second primary waves are generated, the water surface continuously oscillates due to the run-up and run-down of lateral waves along the bank slope, generating additional wave trains.
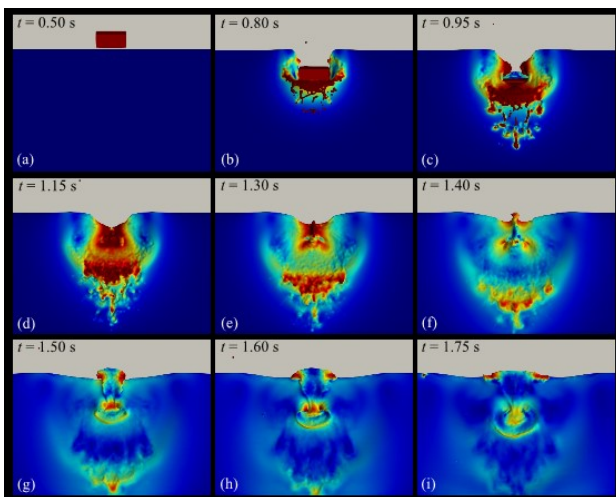
Fig. 8. Generation of the first and second waves in the numerical simulation (Parameters of laboratory test: $b = 0.4$ m, $l = 0.2$ m, $s = 0.1$ m, $v = 2.0$ m/s, $h = 0.29$ m, and $\alpha = 30°$)

4.2.2 Water occupation by the landslide
Based on the above analysis results about the movement features of landslide and water bodies, it is observed that landslides impacting and rapidly occupying water can generate landslide tsunamis. Given the same impact velocity and different α, apparent differences in water occupation volume by landslide and the generated water tongue morphology. In Fig. 9, water bodies are separated by the landslide when it collides into water under all three conditions, forming water tongues splashing toward the opposite bank. Thickness of the water tongue declines with the reduction of α. The water tongue at $\alpha = 30°$ is thicker than that under the other two conditions. As shown in Fig. 9, the second wave formed after the collapse of the air cavity is positively related to α. After the landslide squeezes water bodies, air cavities are formed behind it under all three conditions. Given $\alpha = 30°$ and $20°$, the landslide is immersed in water completely when the air cavity collapses. The length of the landslide cannot affect the development of the second wave. Nevertheless, the landslide enters the water partially when the air cavity collapses under $\alpha = 10°$. As the landslide moves forward continuously, its length hinders the development of the second wave.

The quantity of water body particles in the impacting zone of the landslide before and after impacting into water under three conditions was extracted with the DualSPHysics post-processing tools. On this basis, the occupational volume after the impact of the landslide was acquired. Variations in occupational volume by the landslide with time under all three test conditions are shown in Fig. 10. The rates of water occupation by the landslide after impacting are similar, which are 0.06, 0.056, and 0.050 m³/s under G1, G2, and G3, respectively. When $\alpha = 30°$, the volume of water occupied by the landslide (V_w) is the minimum (0.0446 m³), and it is 5.57 times larger than the volume of the landslide (V_s). When $\alpha = 20°$, $V_w = 0.0546$ m³, and it is 6.83 times larger than V_s. When $\alpha = 10°$, V_w reaches the maximum (0.0633 m³), and it is 7.91 times larger than V_s. The reason is that the landslide has not been completely immersed into water at the air cavity collapse. As the landslide continues to enter water, air is continuously brought into water bodies to displace water.

4.2.3 Wave energy conversion law
The total energy of landslide (E_s) and waves (E_w) in each time step under all three conditions were extracted, respectively. E_w includes the potential energy of wave (E_{pot}) and kinetic energy of wave (E_{kin}). After statistical analysis, the variations in E_s and E_w with time were acquired (Fig. 11). According to observation and comparison, the attenuation rate of E_s increases with α and reaches the lowest at $\alpha = 10°$. Under all three test conditions, when the landslide collides with the water and generates a water tongue, the wave potential energy of the water tongue (E_{pot}) becomes 37.33, 37.54, and 38.01 J, when α increases from $10°$ to $30°$. This result proves that α has no influence on the water tongue height of the landslide-tsunami. According to observation of the first wave generation after the collapse of the water tongue, E_{pot} included in the first wave values are 34.77, 35.78, and 36.93 J when $\alpha = 30°$, $20°$, and $10°$, respectively. This reflects that increasing α leads to a reduction of the first wave. In other words, the first wave crest is negatively related to α. Given the large α, the advancing distance of the landslide on the sliding surface is shorter, and the time for landslide–water interaction is faster, thus decreasing energy conversion between the landslide and the water body. α has great influences on the generation of the second waves. When $\alpha = 30°$, E_{pot} achieves the second growth, and it lasts for a long time. When $\alpha = 20°$, E_{pot} also achieved the second growth, but the increment is small and only lasts for a short period. When $\alpha = 10°$, the water potentials hardly witness the second growth of E_{pot}.
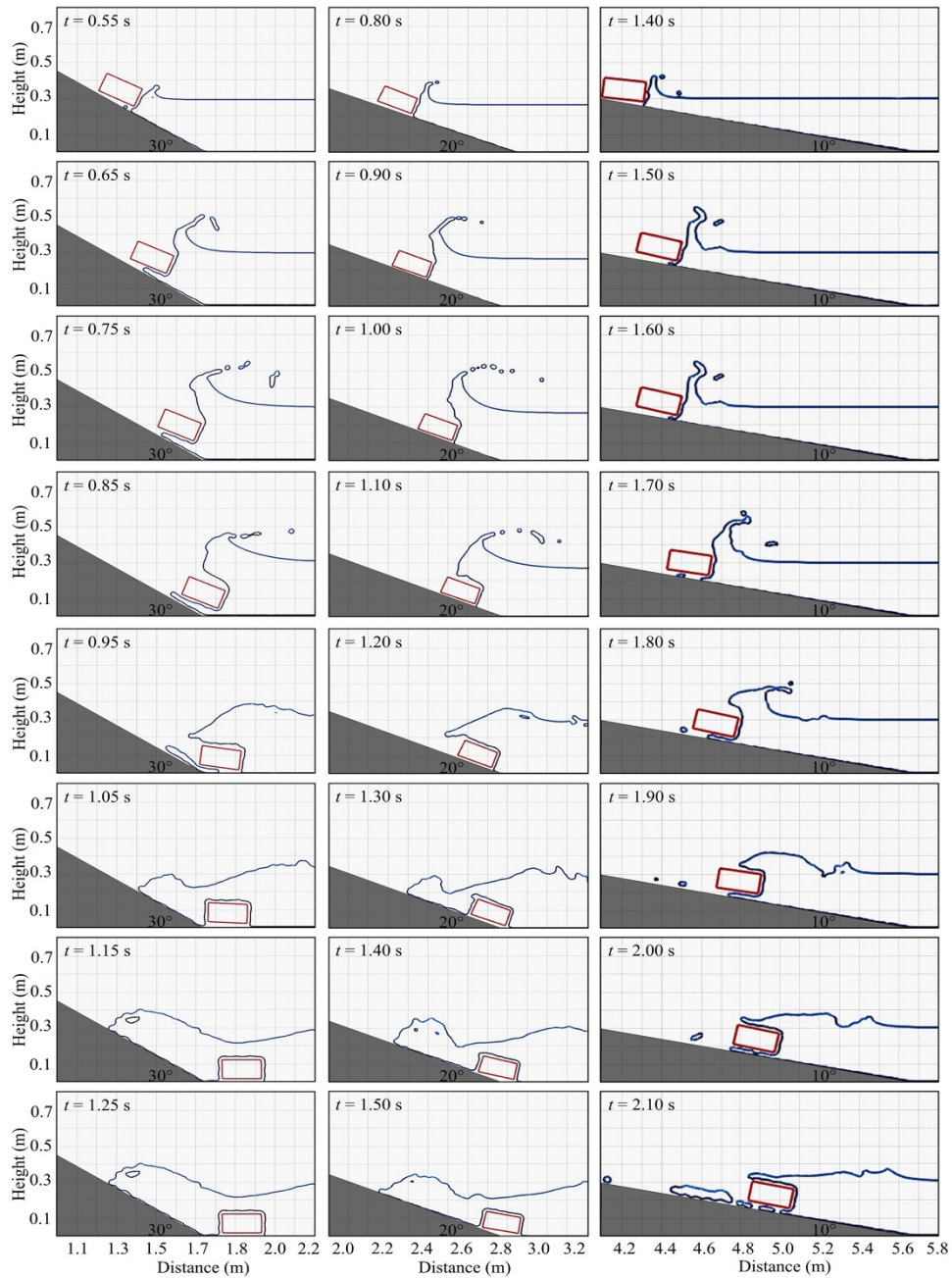
Fig. 9. Occupation process by the landslide under different slide impact angles
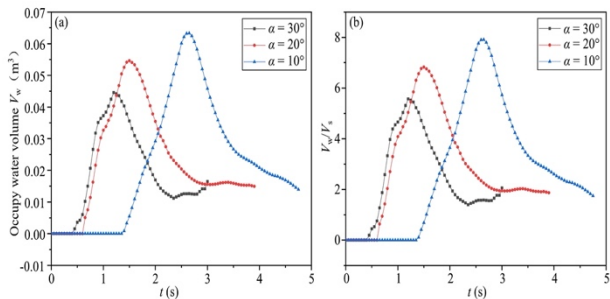
Fig. 10. (a) Variation in the volume of water occupied by the landslide with time; (b) Variation in the rates of water occupation by the landslide with time
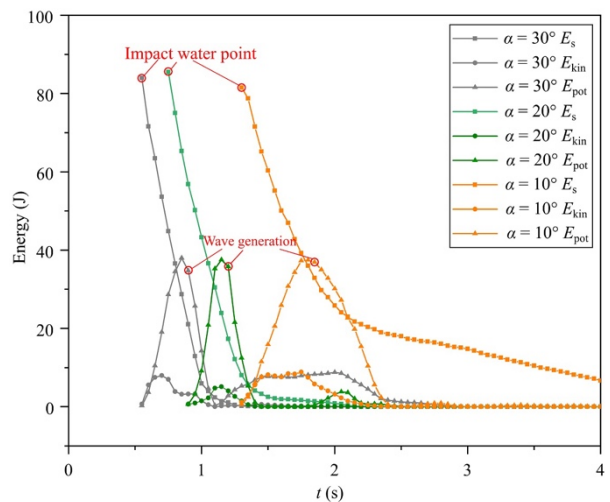
Fig. 11. Variations in landslide energy and water energy in the generation zone of landslide-tsunami with time

5. Conclusion

Three groups of numerical simulation tests are conducted in this study based on the SPH method. The influences of α on landslide-tsunami generation are explored comprehensively from the perspectives of movement features, water occupation by the landslide, and energy conversion law. Some major conclusions could be drawn:

(1) In this study, the SPH method reproduces existing laboratory test results of landslide-tsunami. It is believed that the SPH method is applicable to simulate the generation and propagation of landslide-tsunami. And it achieves high simulation accuracy.

(2) The landslide and water movements are similar under three different slide impact angles. The first waves of landslide-tsunami are formed by the direct impact of landslide onto the water. As the landslide enters the water body and air cavity continuously, the turbulence generated by breaking the air cavity rises toward surrounding areas, generating the second wave. The follow-up wave sequences are formed by water level oscillation when waves run-up and run-down along the banks.

(3) During a landslide into water along the banks, the thickness of the water tongue decreases with the reduction of α. With the increase of α, the rate of water occupation by the landslide increase, but the volume of water occupied by the landslide decreases.

(4) Under different slide impact angles, the energy attenuation rate of landslide in water increases with the increase of α. When there is a very flat bank slope, the energy attenuation rate of the landslide is very low. The first wave crest of landslide-tsunami is negatively related with α, while the second wave crest is positively associated with α.

Based on the above conclusions, the influences of α on different wave trains of landslide-tsunami are entirely opposite. Studying the landslide-tsunami prediction models based on other wave trains is conducive to increasing prediction accuracy of the model. Due to limitations in computing resources, this study only carries out a numerical simulation test by using a single control variable method. A qualitative analysis of the influences of α on the generation of landslide-tsunami is conducted. In the future, multiple groups of numerical simulation tests with different landslide sizes and dynamic parameters could be implemented using computers with stronger computing power to strengthen further quantitative study of influencing the degree of α on landslide-tsunamis.

References

[1] V. Heller and G. Ruffini, "A critical review about generic subaerial landslide-tsunami experiments and options for a needed step change," *Earth-Sci Rev.*, vol. 242, July 2023, Art. no. 104459.
[2] R. Vacondio, P. Mignosa, and S. Pagani, "3D SPH numerical simulation of the wave generated by the Vajont rockslide," *Adv. Water Resour.*, vol.59, pp. 146-156, 2013.
[3] S. S. Gylfadóttir et al., "The 2014 Lake Askja rockslide‐induced tsunami: Optimization of numerical tsunami model using observed data," *J. Geophys. Res. Oceans*, 122, pp. 4110-4122, 2017.
[4] M. P. Lüthi and A. Vieli, "Multi-method observation and analysis of a tsunami caused by glacier calving," *The Cryosphere*, vol. 10, no. 3, pp. 995-1002, 2016.
[5] B. C. McFall, F. Mohammed, H. M. Fritz, and Y. Liu, "Laboratory experiments on three-dimensional deformable granular landslides on planar and conical slopes," *Landslides*, vol. 15, no. 9, pp. 1713-1730, 2018.
[6] R. Sabeti and H. Mohammad. "Semi-empirical predictive equations for the initial amplitude of submarine landslide-generated waves: applications to 1994 Skagway and 1998 Papua New Guinea tsunamis," *Nat. Hazads*, vol. 103, pp. 1591-1611, 2020.
[7] V. Heller and W. H. Hager, "Impulse product parameter in landslide generated impulse waves," *J. Waterw. Port C-Asce.*, vol. 136, pp. 145-155, 2010.
[8] F. M. Evers, H. W. Hager, and R. M. Boes, "Spatial impulse wave generation and propagation," *J. Waterw. Port C-Asce.*, vol. 145, no. 3, pp. 1-15, 2019.
[9] F. Mohammed and H. M. Fritz. "Physical modeling of tsunamis generated by three-dimensional deformable granular landslides," *J. Geophys. Res. Oceans*, vol. 117, no. C11, pp. 3221-3221, 2012.
[10] F. Bregoli, A. Bateman, and V. Medina. "Tsunamis generated by fast granular landslides: 3D experiments and empirical predictors," *J. Hydraul. Res.*, vol. 55, no. 6, pp. 743-758, 2017.
[11] Y. Wang, J. Liu, D. Li, and S. Yan, "Optimization model for maximum tsunami amplitude generated by riverfront landslides based on laboratory investigations," *Ocean Eng.*, vol. 142, pp. 433-440, 2017.
[12] J. W. Kamphuis and R. J Bowering, "Impulse waves generated by landslides," *Coast. Eng.*, pp. 575-588, 1970.
[13] Najafi-Jilani and B. Ataie-Ashtiani, "Estimation of near-field characteristics of tsunami generation by submarine landslide," *Ocean Eng.*, vol. 35, no. 5-6, pp. 545-557, 2008.
[14] R. P. Mulligan and W. A. Take. "On the transfer of momentum from a granular landslide to a water wave," *Coast. Eng.*, vol. 125, pp. 16-22, 2017.
[15] G. K. Bullard, R. P. Mulligan, A. Carreira, and W. A. Take, "Experimental analysis of tsunamis generated by the impact of landslides with high mobility," *Coast. Eng.*, vol. 152, 2019, Art. no. 103538.
[16] B. Huang, Y. Yin, X. Chen, G. Liu, S. Wang, and Z. Jiang. "Experimental modeling of tsunamis generated by subaerial landslides: two case studies of the Three Gorges Reservoir, China," *Environ. Earth Sci.*, vol. 71, no. 9, pp. 3813-3825, 2014.
[17] A. Bougouin, R. Paris, and O. Roche. "Impact of fluidized granular flows into water: Implications for tsunamis generated by pyroclastic flows," *J. Geophys Res. Sol. Ea.*, vol. 125, no. 5, pp. 1-17, 2020.
[18] S. Yavari-Ramshe and B. Ataie-Ashtiani. "On the effects of landslide deformability and initial submergence on landslide-generated waves," *Landslides*, vol. 16, no. 1, pp. 37-53, 2019.
[19] C. Altomare, X. Gironella, and A. J. C. Crespo, "Simulation of random wave overtopping by a WCSPH model," *Appl. Ocean Res.*, vol. 116, 2021, Art. no. 102888.
[20] M. Gomez-Gesteira, B. D. Rogers, A. J. C. Crespo, R. A. Dalrymple, M. Narayanaswamy, and J. M. Dominguez. "SPHysics–development of a free-surface fluid solver–Part 1: Theory and formulations," *Comput. Geosci.*, vol. 48, pp. 289-299, 2012.
[21] M. Gomez-Gesteira, A. J. C. Crespo, B. D. Rogers, R. A. Dalrymple, J. M. Dominguez, and A. Barreiro, "SPHysics–development of a free-surface fluid solver–Part 2: Efficiency and test cases," *Comput. Geosci.*, vol. 48, pp. 300-307, 2012.
[22] J. J. Monaghan, "Smoothed particle hydrodynamics," *Annu. Rev. Astron. Astr.*, vol. 30, no. 1, pp. 543-574, 1992.
[23] J. J. Monaghan and A. Kos, "Scott Russell's wave generator," *Phys. Fluids*, vol. 12, no. 3, pp. 622-630, 2000.
[24] H. Wendland, "Piecewise polynomial, positive definite and compactly supported radial functions of minimal degree," *Adv. Comput. Math.*, vol. 4, pp. 389-396, 1995.

[25] V. Heller, M. Bruggemann, J. Spinneken, and B. D. Rogers, "Composite modelling of subaerial landslide–tsunamis in different water body geometries and novel insight into slide and wave kinematics," *Coast. Eng.*, vol. 109, pp. 20-41, 2016.

[26] R. B. Canelas, J. M. Domínguez, A. J. C. Crespo, M. Gómez-Gesteira, and R. M. L. Ferreira, "A Smooth Particle Hydro-dynamics discretization for the modelling of free surface flows and rigid body dynamics," *Int. J. Numer. Meth. Fl.*, vol. 78, no. 9, pp. 581-593, 2015.

[27] J. Liu *et al.*, "Experimental investigation on near-field edge wave run-ups generated by landslides in narrow reservoirs," *Geol J.*, vol. 58, no. 6, pp. 2268-2282, 2023.